The 0.8-4.5μm broadband transmission spectra of TRAPPIST-1 planets

Ducrot, E.; Sestovic, M.; Morris, B. M.; Gillon, M.; Triaud, A. H. M. J.; Wit, J. de; Thimmarayappa, D.; Agol, E.; Almleaky, Y.; Burdanov, A.; Burgasser, A. J.; Delrez, L.; Demory, B-O; Jehin, E.; Leconte, J.; McCormac, J.; Murray, C.; Queloz, D.; Selsis, F.; Thompson, S.

DOI:
10.3847/1538-3881/aade94

The Astronomical Journal, 156:218 (16pp), 2018 November https://doi.org/10.3847/1538-3881/aade94

The 0.8–4.5 μm Broadband Transmission Spectra of TRAPPIST-1 Planets

E. Ducrot[1], M. Sestovic[2], B. M. Morris[3], M. Gillon[1], A. H. M. J. Triaud[4], J. De Wit[5], D. Thimmarayappa[1], E. Agol[3], Y. Almleaky[6,7], A. Burdanov[1], A. J. Burgasser[8], L. Delrez[9], B-O. Demory[2,10], E. Jehin[1], J. Leconte[11], J. McCormac[12], C. Murray[9], D. Queloz[9], F. Selsis[11], S. Thompson[9], and V. Van Grootel[1]

[1] Space Sciences, Technologies and Astrophysics Research (STAR) Institute, Université de Liége, Allée du 6 Août 19C, B-4000 Liége, Belgium; educrot@uliege.be
[2] University of Bern, Center for Space and Habitability, Gesellschaftsstrasse 6, CH-3012, Bern, Switzerland
[3] Astronomy Department, University of Washington, Seattle, WA 98195 USA
[4] School of Physics & Astronomy, University of Birmingham, Edgbaston, Birmimgham B15 2TT, UK
[5] Department of Earth, Atmospheric and Planetary Science, Massachusetts Institute of Technology, 77 Massachusetts Avenue, Cambridge, MA 02139, USA
[6] Space and Astronomy Department, Faculty of Science, King Abdulaziz University, 21589 Jeddah, Saudi Arabia
[7] King Abdullah Centre for Crescent Observations and Astronomy (KACCOA), Makkah Clock, Saudi Arabia
[8] Center for Astrophysics and Space Science, University of California San Diego, La Jolla, CA, 92093, USA
[9] Cavendish Laboratory, JJ Thomson Avenue, Cambridge, CB3 0H3, UK
[10] University of Copenhagen, Centre for Star and Planet Formation, Niels Bohr Institute and Natural History Museum, DK-1350, Copenhagen, Denmark
[11] Laboratoire d'astrophysique de Bordeaux, Univ. Bordeaux, CNRS, B18N, Allée Geoffroy Saint-Hilaire, F-33615 Pessac, France
[12] Department of Physics, University of Warwick, Gibbet Hill Road, Coventry, CV4 7AL, UK
Received 2018 June 30; revised 2018 August 30; accepted 2018 August 31; published 2018 October 22

Abstract

The TRAPPIST-1 planetary system provides an exceptional opportunity for the atmospheric characterization of temperate terrestrial exoplanets with the upcoming *James Webb Space Telescope* (*JWST*). Assessing the potential impact of stellar contamination on the planets' transit transmission spectra is an essential precursor to this characterization. Planetary transits themselves can be used to scan the stellar photosphere and to constrain its heterogeneity through transit depth variations in time and wavelength. In this context, we present our analysis of 169 transits observed in the optical from space with *K2* and from the ground with the SPECULOOS and Liverpool telescopes. Combining our measured transit depths with literature results gathered in the mid-/near-IR with *Spitzer*/IRAC and *HST*/WFC3, we construct the broadband transmission spectra of the TRAPPIST-1 planets over the 0.8–4.5 μm spectral range. While planet b, d, and f spectra show some structures at the 200–300 ppm level, the four others are globally flat. Even if we cannot discard their instrumental origins, two scenarios seem to be favored by the data: a stellar photosphere dominated by a few high-latitude giant (cold) spots, or, alternatively, by a few small and hot (3500–4000 K) faculae. In both cases, the stellar contamination of the transit transmission spectra is expected to be less dramatic than predicted in recent papers. Nevertheless, based on our results, stellar contamination can still be of comparable or greater order than planetary atmospheric signals at certain wavelengths. Understanding and correcting the effects of stellar heterogeneity therefore appears essential for preparing for the exploration of TRAPPIST-1 with *JWST*.

Key words: binaries: eclipsing – planetary systems – techniques: photometric – techniques: spectroscopic

1. Introduction

The nearby (∼12 pc) TRAPPIST-1 system is composed of an M8-type dwarf star orbited by seven nearly Earth-sized, temperate, planets (Gillon et al. 2017, hereafter G17). Considering their transiting nature, combined with the infrared brightness ($K = 10.3$) and the Jupiter-like size of their host star (∼0.12 $R_\odot$, Van Grootel et al. 2018), these planets are particularly promising candidates for the first thorough atmospheric characterizations of temperate terrestrial worlds with the upcoming *James Webb Space Telescope* (*JWST*) (G17, Barstow & Irwin 2016; Morley et al. 2017). However, some recent works proposed that an inhomogeneous stellar photosphere—as anticipated for red dwarfs like TRAPPIST-1—could strongly complicate the information content of the exoplanets' transmission spectra, limiting the deciphering of their atmospheric properties (Apai et al. 2018; Rackham et al. 2018, hereafter R18). Therefore, the quantification and the correction of this spectral contamination should be a critical preliminary step before any intensive follow-up of the planets with *JWST*.

From TRAPPIST-1's *K2* variability, R18 estimated TRAPPIST-1's coverage to be 8^{+18}_{-7}% of cold spots and 54^{+16}_{-46}% of hot faculae, assuming solar-type spots (which maximize the impact on the planets' transit spectra). They concluded that such a strong heterogeneous photosphere could alter the transit depth of the planets by roughly 1–15 times the strength of planetary features, dramatically complicating follow-up observations with *JWST*. More recently, Zhang et al. (2018, hereafter Z18) analyzed the near-IR data obtained with *HST*/WFC3 for several TRAPPIST-1 planets, and compared their resulting transit spectra with the R18 stellar contamination model. They concluded that the star should be almost entirely covered by spots (∼30%) and faculae (∼63%)—essentially a "two-component photosphere"—and predicted dramatic (a few dozens of percent) chromatic variations of the transit depths, especially in the optical.

In this context, here we present our analysis of 169 transit light curves observed in the optical by the *K2* (Luger et al. 2017), SPECULOOS (Burdanov et al. 2017; Gillon 2018), and Liverpool (Steele et al. 2004) telescopes. We combine our measurements with the ones obtained in the mid-IR by *Spitzer*/IRAC (Delrez et al. 2018) and in the near-IR by *HST*/WFC3 (de Wit et al. 2018) to construct the broadband transmission spectra of the TRAPPIST-1 planets over the 0.8–4.5 μm spectral range. We confront these spectra with stellar

Table 1
Number of Transits Observed by *K2*, SSO, and LT Analyzed in this Work for Each TRAPPIST-1 Planet

Planet	*K2*	SSO	LT
TRAPPIST-1 b	42	20	4
TRAPPIST-1 c	29	11	5
TRAPPIST-1 d	15	5	1
TRAPPIST-1 e	8	8	2
TRAPPIST-1 f	6	2	/
TRAPPIST-1 g	3	3	/
TRAPPIST-1 h	1	3	1

contamination models in order to assess the impact of the heterogeneity of the star's photosphere on the atmospheric characterization of its planets.

The new observations and their reduction are described in Section 2, where we also provide our detailed data analysis and results. In Section 3 we discuss the temporal variability of the measured transit depths, as well as the structure of the planets' broadband transit transmission spectra, notably leveraging the visible part of these spectra for the first time. We present two different scenarios capable of fitting the spectra, and for which stellar heterogeneity could be dominated by a few giant cold spots or a few small hot faculae, and discuss their implications for the atmospheric characterization of the planets. Finally, we give our conclusions in Section 4.

2. Observations and Data Analysis

2.1. Observations

The new data used in this work consist of transit light curves of the TRAPPIST-1 planets observed from the ground by the SPECULOOS (Gillon 2018) and Liverpool (Steele et al. 2004) telescopes and from space by the *K2* mission (Howell et al. 2014).

We observed 37 different transits with 1 or 2 telescopes of the SPECULOOS-South Observatory (SSO, Burdanov et al. 2017; Gillon 2018) at Cerro Paranal, Chile (see Table 1), in the context of the commissioning of the facility. This represents 52 transits in total, as some were observed with two SSO telescopes simultaneously. Each SSO robotic telescope has a primary aperture of 1 m and a focal length of 8 m, and is equipped with a $2k \times 2k$ deep-depletion CCD camera whose 13.5 μm pixel size corresponds to 0.″35 on the sky (field of view $= 12' \times 12'$). These observations were carried out in an $I+z$ filter for which we computed an effective wavelength of $\sim$0.9 μm for a M8-type star like TRAPPIST-1, taking into account the spectral response curve of the telescope +atmosphere. Exposure times of 23 s were used for all observations. A standard calibration (bias, dark, and flat-field corrections) was applied to each image, and fluxes were measured for the stars in the field with the DAOPHOT aperture photometry software (Stetson 1987). Differential photometry was then performed after a careful selection of comparison stars.

We obtained 13 transits of the TRAPPIST-1 planets with the use of the 2 m Liverpool Telescope (LT, Steele et al. 2004) installed on the island of La Palma at the Roque de los Muchachos observatory. For our observations, we used the IO:O optical wide field camera which has $4k \times 4k$ deep-depletion CCD with 15 μm sized pixels and 10×10 arcmin^2 field of view. We used 2×2 binning that resulted in a 0.3 arcsec pixel^{-1} image scale. All the observations were performed in the Sloan z' band with 20 s exposures. Data reduction and subsequent aperture photometry were carried out in the same manner as for the SSO data.

TRAPPIST-1 was observed with the *K2* telescope in an overall bandpass ranging from 420 to 900 nm over a period of 79 days in Campaign 12, which represents a total of 104 transits. The short cadence Target Pixel File (TPF), with a cadence rate of 1 per minute, was downloaded from the Mikulski Archive for Space Telescopes (MAST). We used the same procedure to extract and detrend the light curve as done in Luger et al. (2017) and Grimm et al. (2018). We first applied a centroiding algorithm to find the (x, y) position of the PSF center in each cadence frame. We summed the flux within a circular top-hat aperture, centered on the PSF center in each frame. We used a Gaussian Process regression pipeline (Luger et al. 2017; Grimm et al. 2018) to remove the instrumental systematics due to *K2* telescope's periodic roll angle drift, and the stellar variability. The systematics were fitted using a kernel that contained additive terms for the time- and position-dependent variation, enabling us to separate and subtract them individually. To ensure that the transits were not fitted as stellar variability, we masked them out during the fitting and regression procedure. The stellar and long-term variability were then subtracted from the light curve. The 6 hr combined differential photometric precision (CDPP) of the detrended light curve is 339 ppm.

We considered only well-isolated and complete transits in our analysis, discarding blended transits of different planets (nine transits discarded), partial transits (six transits discarded), transits affected by flares (seven transits discarded), and transits affected by technical problems or bad weather conditions (three transits discarded). In total, 35 transits were discarded. Our final data set was composed of 169 transit light curves, respectively 67 for TRAPPIST-1 b, 45 for -1 c, 21 for -1 d, 18 for -1 e, 8 for -1 f, 7 for -1 g, and 5 for -1 h. The number of transits kept for each planet is presented in Table 1 for *K2*, SSO, and LT.

2.2. Data Analysis

We chose to follow different approaches in our data analysis to ensure the robustness of our results. First, we analyzed each transit individually to extract its individual properties to, notably, search for signs of variability. Then, we proceeded to a global analysis of all transit light curves for each planet to determine precisely the average transit depths in *K2*, SSO, and LT bandpass. Finally, we performed an additional global analysis, this time enabling all transits to have different depths in order to assess their variability. For those two distinct global analyses, the transits observed by *K2*, SSO, and LT were analyzed separately. All of our analyses were performed with the most recent version of the adaptive Markov Chain Monte-Carlo (MCMC) code introduced in Gillon et al. (2012; see Gillon et al. 2014, hereafter G14, for an extensive description of our MCMC algorithm). In this work we assumed a quadratic limb-darkening (LD) law for all the analyses, using normal prior distributions for the LD coefficients u_1 and u_2 based on theoretical values and 1σ errors interpolated from the table of Claret & Bloemen (2011). The modes of the normal prior distributions for u_1 and u_2 for the non-conventional $I+z$ filter

Table 2
Comparison of $dF_{\rm Analyses}$, the Transit Depth Values Obtained from a Global Analysis of all the *K2* Transits for Each Planet, with $dF_{\rm LD}$, the Transit Depth Values Obtained from a Global Analysis of the Period-folded TTV-corrected *K2* Transit Photometry with Free Limb-darkening Coefficients for All Planets

Telescope	Planet	$dF_{\rm LD}$ (%)	$dF_{\rm Analyses}$ (%)
K2	1b	0.751 ± 0.027	0.716 ± 0.021
	1c	0.712 ± 0.009	0.684 ± 0.019
	1d	0.386 ± 0.009	0.412 ± 0.028
	1e	0.460 ± 0.009	0.449 ± 0.034
	1f	0.617 ± 0.067	0.541 ± 0.034
	1g	0.741 ± 0.026	0.668 ± 0.070
	1h	0.291 ± 0.029	0.347 ± 0.058

used by SSO were chosen as the average of the values interpolated from the tables for the standard filters I_c and z'.

Finally, for each instrument we also performed a global analysis of all transits for each planet with free LD coefficients, those values being the same across all planets within each global analysis. The aim of this analysis was to better constrain the limb-darkening coefficients, as each planet samples a different chord of the stellar photosphere. For *K2*, the fitted LD coefficients through this procedure are consistent with the model-based LD priors used in the other analyses, the output LD coefficients from this global analysis were successfully constrained by the many transits. In this case, their respective values were: $u1 = 1.00 + -0.1$; $u2 = -0.04 + -0.2$ whereas the priors used on the LD coefficients in the rest of our analyses from interpolation of Claret & Bloemen (2011) tables were $u1 = 0.99 + -0.09$; $u2 = -0.19 + -0.08$, which is consistent. The transit depths derived from this analysis are consistent with the remainder of our analyses (Table 2). Unfortunately, for SSO and LT these global analyses failed to converge, meaning that the data do not allow for the constraint of the limb=darkening coefficients.

2.2.1. Individual Analyses of the Light Curves

First, we converted for each photometric measurement the mid-exposure time to the $\rm BJD_{TDB}$ time system, as recommended by Eastman et al. (2010). We modeled each transit with the model of Mandel & Agol (2002), multiplied by a baseline model accounting for the photometric variations of stellar, atmospheric, and instrumental origins (see G14). For each light curve, the model selection was based on the minimization of the Bayesian Information Criterion (BIC, Schwarz 1978). For a significant fraction of the light curves obtained by *K2* and SSO, including a polynomial function of time in the model—to account for the low-frequency signals like the rotational variability of the star—resulted in a significant decrease of the BIC (see Table 3). For some SSO and LT light curves, additional terms in the position or width of the stellar point-spread function were also favored (see Tables 4 and 5). A small fraction of the SSO's light curves' baselines also included an airmass and/or a background polynomial function.

For each transit light curve, the jump parameters of the MCMC analysis, i.e., the parameters perturbed at each step of the Markov chains, were as follows:

1. The transit depth (planet-to-star area ratio) $dF = (R_p/R_\star)^2$, the time of mid-transit (or inferior conjunction) T_0, and the transit impact parameter assuming a circular orbit $b = a\cos i/R_\star$, where a is the semimajor axis and i is the inclination of the orbit.
2. The mass, radius, effective temperature, and metallicity of the star, for which we assumed the following normal prior distributions: $M_\star = 0.089 \pm 0.006\,M_\odot$, $R_\star = 0.121 \pm 0.003\,R_\odot$, $T_{\rm eff} = 2516 \pm 41$ K, and $[{\rm Fe/H}] = 0.04 \pm 0.08$ (Van Grootel et al. 2018), respectively.

We first assessed a correction factor (CF) for each individual light curve via a short (10,000 steps) Markov chain. This correction factor was then used to rescale the photometric error bars while accounting for a possible inadequate estimation of the white noise (βw) and the presence of red noise (βr) via $\rm CF = \beta_w * \beta_r$. β_r allows us to account for possible correlated noise present in the light curve; this scaling factor is determined by following a procedure similar to the one described in Winn et al. (2008) in which it is obtained by comparing the standard deviations of the binned and unbinned residuals for different binning intervals ranging from 5 to 120 minutes, i.e., the typical timescales of an eclipse light curve (e.g., the duration of ingress or egress).

We then ran 2 chains of 100,000 steps for each light curve and successfully tested their convergence using a statistical test of Gelman & Rubin (1992).

The results obtained from these individual analyses are shown in Table 6 for SSO, in Table 7 for *K2*, and in Table 8 for LT. Each table gathers for each planet the transit times and depths derived from these individual analyses. The results are discussed in Section 3.

2.2.2. Global Analyses

Our next step was to perform, for each planet and for each data set (*K2*, SSO, and LT), a global analysis of all transit light curves, to better separate the actual transit signals from the correlated noise of similar frequencies, and thus to improve the accuracies of the derived transit depths.

These global analyses were done in two steps. First, for each planet and each instrument (*K2*, SSO, and LT), a general global analysis of all the transits with common transit shape parameters was performed, followed by a global analysis allowing for transit depth variations.

We used the same priors on the stellar parameters as reported in Section 2.2.1. However, in this global analysis, we set a transit timing variation (TTV) as a jump parameter for each transit, fixing the planetary periods P and reference transit timings T_0 to those reported in Delrez et al. (2018). This global analysis includes 6 shared parameters across transits (the stellar parameters M_*, $T_{\rm eff}$, R_*, [Fe/H] + limb-darkening coefficients): for each planet the individual parameters are *df* and *b*, and have the same number of TTVs as transits.

For each transit, we assumed the baseline model derived from the individual analysis, following the same procedure to rescale the photometric error bars, and derived our parameter estimates from the posterior distributions obtained from two Markov chains of 100,000 steps, with a 25% burn-in phase, whose convergence was checked using the Gelman & Rubin (1992) test. The transit depths obtained for each data set are displayed in Table 9.

In a second step, we performed similar global MCMC analyses, but this time with the depths of all individual transits as jump parameters for all three instruments (*K2*, SSO, and LT). The aim here was to benefit from the constraint brought by

Table 3
Same as Table 4, but for *K2*

Planet	Date	Number of Points	Epoch	Baseline	β_w	β_r	CF
b	2016 Dec 18	301	277	$p(t^2)$	0.86	1.84	1.59
	2016 Dec 20	303	278	$p(t^3)$	0.88	1.68	1.47
	2016 Dec 21	303	279	$p(t^1)$	0.82	1.08	0.95
	2016 Dec 23	304	280	$p(t^1)$	0.84	1.00	0.84
	2016 Dec 26	242	282	$p(s)$	0.91	1.11	1.01
	2016 Dec 27	241	283	$p(s)$	0.92	1.08	1.00
	2016 Dec 29	305	284	$p(t^2)$	0.91	1.38	1.26
	2016 Dec 30	304	285	$p(s)$	0.84	1.34	1.13
	2017 Jan 01	303	286	$p(t^2)$	0.86	1.01	0.87
	2017 Jan 02	305	287	$p(t^1)$	0.90	1.74	1.57
	2017 Jan 04	303	288	$p(s)$	0.80	1.74	1.40
	2017 Jan 05	214	289	$p(t^1)$	0.81	1.00	1.81
	2017 Jan 07	302	290	$p(t^3)$	0.87	1.15	1.01
	2017 Jan 08	269	291	$p(t^3)$	0.93	1.09	1.02
	2017 Jan 10	303	292	$p(s)$	0.87	1.82	1.57
	2017 Jan 11	303	293	$p(t^3)$	0.84	1.07	0.91
	2017 Jan 13	305	294	$p(t^1)$	0.89	1.12	1.00
	2017 Jan 14	305	295	$p(t^2)$	0.90	1.28	1.16
	2017 Jan 16	297	296	$p(s)$	0.91	1.63	1.49
	2017 Jan 17	215	297	$p(t^1)$	0.84	1.53	1.28
	2017 Jan 19	206	298	$p(s)$	0.82	1.68	1.39
	2017 Jan 20	259	299	$p(s)$	0.92	1.22	1.13
	2017 Jan 22	304	300	$p(t^1)$	0.88	1.48	1.32
	2017 Jan 23	303	301	$p(t^4)$	0.89	1.00	0.89
	2017 Jan 25	302	302	$p(s)$	0.82	1.19	0.87
	2017 Jan 26	302	303	$p(t^1)$	0.86	1.43	1.23
	2017 Jan 29	293	305	$p(t^2)$	0.87	1.04	0.91
	2017 Jan 31	304	306	$p(t^3)$	0.90	1.22	1.11
	2017 Feb 07	306	311	$p(t^3)$	0.81	1.09	0.87
	2017 Feb 10	300	313	$p(s)$	0.97	1.63	1.58
	2017 Feb 12	304	314	$p(s)$	1.04	1.31	1.36
	2017 Feb 13	302	315	$p(t^4)$	0.92	1.12	1.03
	2017 Feb 15	304	316	$p(t^2)$	0.94	1.34	1.26
	2017 Feb 16	303	317	$p(t^3)$	0.94	1.16	1.09
	2017 Feb 18	296	318	$p(t^1)$	0.81	1.09	0.87
	2017 Feb 19	305	319	$p(t^1)$	0.88	1.11	0.98
	2017 Feb 21	206	320	$p(s)$	0.91	1.54	1.40
	2017 Feb 24	294	322	$p(t^1)$	0.95	1.08	1.02
	2017 Feb 26	305	323	$p(t^3)$	0.87	1.00	0.87
	2017 Mar 01	196	325	$p(s)$	0.95	1.19	1.13
	2017 Mar 01	291	326	$p(t^1)$	0.93	1.00	0.93
	2017 Mar 04	305	327	$p(s)$	1.02	1.89	1.93
c	2016 Dec 18	304	189	$p(t^1)$	0.83	1.00	0.83
	2016 Dec 20	219	190	$p(t^2)$	0.87	1.28	1.07
	2016 Dec 22	217	191	$p(s)$	0.81	1.73	1.41
	2016 Dec 25	304	192	$p(s)$	0.86	1.64	1.41
	2016 Dec 27	238	193	$p(s)$	0.83	1.00	0.83
	2016 Dec 30	303	194	$p(t^1)$	0.80	1.30	1.04
	2017 Jan 03	232	196	$p(s)$	0.89	2.14	1.90
	2017 Jan 05	185	197	$p(t^1)$	0.89	1.06	0.94
	2017 Jan 07	250	198	$p(t^4)$	0.88	1.22	1.08
	2017 Jan 11	304	199	$p(s)$	0.85	1.51	1.28
	2017 Jan 13	302	200	$p(s)$	0.84	1.35	1.14
	2017 Jan 16	249	201	$p(t^2)$	0.81	1.25	1.03
	2017 Jan 18	244	202	$p(s)$	0.80	1.09	0.87
	2017 Jan 20	284	203	$p(t^1)$	0.84	1.17	0.98
	2017 Jan 23	305	204	$p(t^3)$	0.86	1.00	0.86
	2017 Jan 25	304	205	$p(s)$	0.91	1.46	1.34
	2017 Jan 27	233	206	$p(s)$	0.84	1.29	1.08
	2017 Jan 30	216	207	$p(t^1)$	0.91	1.13	1.03
	2017 Feb 06	188	210	$p(t^3)$	0.85	1.00	0.85
	2017 Feb 09	221	211	$p(t^1)$	0.87	1.31	1.14
	2017 Feb 11	303	212	$p(t^2)$	0.88	1.18	1.05

Table 3
(Continued)

Planet	Date	Number of Points	Epoch	Baseline	β_w	β_r	CF
	2017 Feb 14	304	213	$p(t^3)$	0.85	1.77	1.51
	2017 Feb 16	258	214	$p(t^2)$	0.95	1.69	1.60
	2017 Feb 18	253	215	$p(t^3)$	0.85	1.11	1.94
	2017 Feb 21	210	216	$p(t^1)$	0.92	1.42	1.31
	2017 Feb 23	307	217	$p(t^2)$	0.89	1.31	1.17
	2017 Feb 26	304	218	$p(s)$	0.89	2.00	1.79
	2017 Feb 28	306	219	$p(t^2)$	0.93	1.00	0.93
	2017 Mar 03	305	220	$p(t^3)$	0.87	1.00	0.87
d	2016 Dec 16	305	44	$p(s)$	0.84	1.13	0.96
	2016 Dec 20	203	45	$p(t^4)$	0.79	1.00	0.79
	2016 Dec 28	304	47	$p(t^4)$	0.88	1.13	1.00
	2017 Jan 01	186	48	$p(t^1)$	0.83	1.00	0.83
	2017 Jan 05	198	49	$p(s)$	0.89	1.01	0.90
	2017 Jan 09	305	50	$p(t^3)$	0.79	1.00	0.79
	2017 Jan 13	304	51	$p(t^1)$	0.84	1.09	0.91
	2017 Jan 17	491	52	$p(s)$	0.91	1.48	1.35
	2017 Jan 21	306	53	$p(t^1)$	0.87	1.30	1.13
	2017 Jan 25	298	54	$p(t^3)$	0.87	1.45	1.27
	2017 Feb 07	210	57	$p(s)$	0.87	1.00	0.87
	2017 Feb 23	305	61	$p(t^1)$	0.87	1.11	0.97
	2017 Feb 27	304	61	$p(t^1)$	0.93	1.40	1.30
	2017 Mar 03	306	63	$p(s)$	0.97	1.00	0.97
e	2016 Dec 17	259	70	$p(t^1)$	0.84	1.40	1.17
	2016 Dec 23	303	71	$p(t^1)$	0.87	1.27	1.11
	2016 Jan 04	296	73	$p(t^1)$	0.88	2.01	1.78
	2016 Jan 10	251	74	$p(t^1)$	0.89	1.20	1.08
	2016 Jan 16	306	75	$p(t^1)$	0.87	1.04	0.90
	2016 Jan 22	304	76	$p(t^2)$	0.83	1.05	0.89
	2016 Jan 28	304	77	$p(t^1)$	0.91	1.00	0.91
	2016 Feb 10	304	79	$p(t^1)$	0.90	1.55	1.40
f	2016 Dec 22	260	8	$p(s)$	0.90	1.52	1.37
	2016 Dec 31	304	9	$p(s)$	0.88	1.16	1.03
	2017 Jan 09	304	10	$p(s)$	0.90	1.79	1.62
	2017 Jan 19	223	11	$p(t^1)$	0.89	1.15	1.03
	2017 Feb 15	303	14	$p(s)$	0.87	1.67	1.46
	2017 Feb 15	301	15	$p(s)$	0.89	1.30	1.15
g	2017 Jan 10	199	8	$p(s)$	0.89	1.05	0.93
	2017 Feb 16	256	11	$p(t^1)$	0.88	1.51	1.34
	2017 Mar 01	156	12	$p(s)$	0.96	1.41	1.35
h	2017 Jan 02	304	5	$p(t^1)$	0.82	1.06	0.88

the common transit shape (duration, impact parameter) to derive more accurate individual transit depths, and thus to better assess their potential variability. This time the analysis includes four shared parameters across transits (the stellar parameters M_*, $T_{\rm eff}$, R_*, [Fe/H]): for each planet there are as many individual transit depths as there are transits plus the impact parameter (limb-darkening coefficients are fixed), and the same number of TTVs as transits.

Tables 10–12 present our measured transit depths as deduced from our global analyses of SSO, *K2*, and LT transits, respectively. Their temporal evolution is shown for each planet in Figure 1 (we did not plot Liverpool data because of the small number of light curves, but the values can be found in Table 12). For further comparison, these figures also display the medians of the global MCMC posterior probability distribution functions (PDFs) as measured with *Spitzer* at 4.5 μm by Delrez et al. (2018), and also the PDF derived from the MCMC analyses assuming common transit depths.

We compared the results obtained from the individual and global analyses of the transits and found them to be fully consistent. Accurately constraining of the transit shape through a global analysis slightly improves the errors on the depths or timings for some transits, while others have larger errors due to the clearer separation between signal and red noise. For this reason, we adopt the results of our global analyses as our final ones.

3. Results and Discussion

3.1. Temporal Evolution of the Transit Depths

Changes in the transit depths measured for a planet in a given bandpass could result from the evolution of stellar

Table 4
Description of the Transit Light Curves Measured for TRAPPIST-1 Planets by SPECULOOS-South

Planet	Date	Telescope	Number of Points	Epoch	Baseline	β_w	β_r	CF
b	2017 Jun 18	Europa	487	398	$p(\mathrm{fwhm}^1)$	1.22	1.20	1.47
	2017 Jun 30	Io	196	406	$p(t^1)$	1.04	1.00	1.04
	2017 Jun 30	Europa	242	406	$p(t^1) + p(xy^1)$	1.02	1.89	1.93
	2017 Aug 01	Europa	273	427	$p(\mathrm{fwhm}^1)$	1.28	1.09	1.40
	2017 Aug 07	Europa	228	431	$p(\mathrm{fwhm}^1)$	1.07	1.49	1.59
	2017 Aug 13	Europa	263	435	$p(t^1)$	1.18	1.18	1.39
	2017 Aug 13	Io	434	435	$p(t^1)$	1.04	1.15	1.19
	2017 Aug 19	Europa	287	439	$p(s)$	1.09	1.24	1.35
	2017 Aug 25	Europa	284	443	$p(s)$	1.35	1.3	1.75
	2017 Sep 20	Europa	254	460	$p(t^1) + p(xy^1)$	1.29	1.04	1.33
	2017 Sep 23	Io	264	462	$p(xy^1)$	0.99	1.30	1.30
	2017 Oct 08	Europa	257	472	$p(xy^1)$	1.3	1.3	1.69
	2017 Oct 20	Europa	227	480	$p(t^1)$	1.06	1.2	1.28
	2017 Nov 30	Europa	260	507	$p(s)$	1.22	1.21	1.48
	2017 Nov 30	Io	267	507	$p(t^1) + p(\mathrm{fwhm}^1)$	1.21	1.00	1.21
	2017 Dec 03	Io	262	509	$p(t^1)$	1.13	1.37	1.55
	2017 Dec 03	Europa	259	509	$p(t^1)$	1.04	1.00	1.04
	2017 Dec 06	Europa	212	511	$p(t^1)$	1.89	1.00	1.89
	2017 Aug 28	Europa	154	445	$p(s)$	1.13	1.07	1.21
	2017 Aug 28	Io	156	445	$p(s)$	1.16	1.00	1.16
c	2017 Aug 28	Europa	178	294	$p(\mathrm{fwhm}^1)$	1.14	1.00	1.14
	2017 Aug 28	Io	272	294	$p(t^1)$	1.10	1.61	1.76
	2017 Sep 14	Europa	247	301	$p(t^1)$	1.08	1.35	1.45
	2017 Sep 15	Io	339	301	$p(t^1) + p(a^1)p(\mathrm{fwhm}^1)$	1.95	1.00	1.95
	2017 Oct 06	Europa	364	310	$p(t^2)$	1.12	1.19	1.33
	2017 Oct 18	Europa	264	315	$p(t^1)$	1.13	1.04	1.18
	2017 Nov 21	Europa	318	329	$p(b^1)$	1.14	1.21	1.37
	2017 Nov 21	Io	265	329	$p(t^1) + p(\mathrm{fwhm}^1)$	1.07	1.37	1.47
	2017 Dec 08	Europa	240	336	$p(s)$	1.11	1.18	1.31
	2017 Dec 08	Io	243	336	$p(a^1)$	1.08	1.27	1.38
	2017 Nov 04	Europa	267	322	$p(t^1)$	1.19	1.00	1.19
d	2017 Jul 26	Europa	422	72	$p(s)$	1.03	1.78	1.82
	2017 Aug 03	Europa	325	74	$p(t^1)$	1.18	1.31	1.55
	2017 Aug 03	Io	378	74	$p(t^1) + p(\mathrm{fwhm}^1)$	1.16	1.38	1.59
	2017 Aug 07	Europa	320	75	$p(t^1) + p(\mathrm{fwhm}^1)$	1.17	1.00	1.17
	2017 Oct 07	Europa	322	90	$p(t^1) + p(xy^1)$	1.07	1.13	1.21
e	2017 Jun 29	Europa	422	45	$p(s)$	1.19	1.00	1.19
	2017 Jun 29	Io	401	45	$p(t^1)$	1.06	1.33	1.41
	2017 Jul 05	Europa	448	46	$p(a^1) + p(\mathrm{fwhm}^1)$	1.44	1.10	1.58
	2017 Jul 05	Io	445	46	$p(t^2) + p(\mathrm{fwhm}^1)$	1.13	1.00	1.13
	2017 Aug 17	Europa	388	53	$p(s)$	0.93	1.39	1.30
	2017 Aug 17	Io	198	53	$p(s)$	0.91	1.05	0.95
	2017 Aug 23	Europa	418	54	$p(s)$	1.14	1.82	2.08
	2017 Aug 23	Io	415	54	$p(s)$	1.14	1.35	1.53
f	2017 Aug 27	Europa	363	35	$p(s)$	1.14	1.55	1.76
	2017 Oct 10	Europa	608	40	$p(s)$	1.11	1.42	1.58
g	2017 Jun 19	Europa	497	21	$p(\mathrm{fwhm}^1)$	0.95	1.05	1.00
	2017 Jul 26	Europa	475	22	$p(s)$	1.24	1.48	1.83
	2017 Jul 27	Europa	533	23	$p(s)$	1.23	1.08	1.34
h	2017 Jul 27	Europa	741	16	$p(a^1)$	1.28	1.70	2.18
	2017 Aug 15	Io	412	17	$p(t^1)$	1.01	1.08	1.19
	2017 Aug 15	Europa	434	17	$p(a^1)$	0.97	1.81	1.77

Note. For each light curve, this table shows the date of acquisition, the instrument used, the number of data points, the epoch based on the transit ephemeris presented in Delrez et al. (2018), the selected baseline function (see Section 2), and the deduced values for β_w, β_r, and CF $= \beta_r * \beta_w$ (see Section 2). For the baseline function, $p(\epsilon^N)$ denotes, respectively, an N-order polynomial function of time ($\epsilon = t$), the full width at half maximum ($\epsilon =$ fwhm), x and y positions ($\epsilon = xy$), the background ($\epsilon = b$), the airmass ($\epsilon = a$), and a scalar ($\epsilon = s$).

Table 5
Same as Table 4, but for LT

Planet	Date	Number of Points	Epoch	Baseline	β_w	β_r	CF
b	2017 May 31	139	386	$p(t^1) + p(\mathrm{fwhm}^1)$	1.23	1.00	1.23
	2017 Jul 23	152	421	$p(s)$	1.00	1.09	1.09
	2017 Jul 29	153	425	$p(s)$	0.99	1.08	1.07
	2017 Aug 5	156	429	$p(t^1)$	1.58	1.00	1.58
c	2017 Jul 01	157	270	$p(s)$	0.88	1.43	1.26
	2017 Sep 07	178	298	$p(t^1))$	0.95	1.00	0.95
	2017 Sep 19	178	303	$p(t^1)$	1.31	1.24	1.63
	2017 Oct 28	176	319	$p(s)$	1.11	1.31	1.46
	2017 Aug 5	187	284	$p(s)$	1.51	1.25	1.79
d	2017 Sep 21	227	113	$p(t^1) + p(\mathrm{fwhm}^1)$	1.45	1.05	1.52
e	2017 Aug 17	274	110	$p(t^1)$	1.30	1.28	1.66
	2017 Aug 17	202	118	$p(s)$	1.00	1.55	1.55
h	2017 Aug 15	378	17	$p(t^1)$	1.00	1.00	1.00

heterogeneities on or outside the chord transited by the planet. Figure 1 shows the evolution of the transit depths derived from our global analyses of *K2* and SSO light curves. These analyses assumed a common transit profile—except for the depths—for each planet and each instrument to better separate the correlated noise from the transit signals and thus guarantee robust results on the transit depths. From those results, we noticed that for all planets the depths are consistent from one transit to another, with no discrepancy larger than 3σ. We computed the standard deviation of the measurements and compared it to the mean value of the measurement errors for each data set; the values are presented in Table 13.

We found that the standard deviation is consistent with the mean of the measurements errors for most of the planet/instrument associations. The exceptions are planet c (SSO, LT) and planet d (*K2*), where the dispersion of the measurements is actually larger than the mean errors. These mild discrepancies could be genuine, but they could also originate from small-number statistics. Indeed, only 4 transits are used to compute the statistics for LT, 11 transits are used for SSO for planet c, and 10 transits are used for planet d.

Looking at the few transits that were observed simultaneously with *Spitzer* (values from Delrez et al. 2018) and *K2* (see Table 7) on one hand and with SPECULOOS (see Table 6) and LT (see Table 8) on the other hand, we see that the transit depth values are in agreement with one another (see Table 14), with *K2* error bars being significantly larger than *Spitzer* error bars. For certain transits, the value derived from *K2* is larger than the one derived from *Spitzer*, while for others it is the opposite. We can conclude on the transit observed simultaneously by SPECULOOS and the Liverpool telescope, as it is unique.

3.2. Transmission Spectra of the TRAPPIST-1 Planets

Combining the results of our analyses to the ones presented by Delrez et al. (2018) for *Spitzer* measurements and by de Wit et al. (2018) for *HST*/WFC3 measurements, we construct the broadband 0.8–4.5 μm transit transmission spectra of TRAPPIST-1 planets (Figure 2).

We first note that although the measurements obtained with the *HST* data do not show features over the WCF3 band (1.1–1.7 μm), the transit depths are significantly deeper than those obtained at other wavelengths for planets b and d. Although this is intriguing, these deeper transits could very well have an instrumental origin. Indeed, as *HST* is on a low-Earth orbit, it can monitor TRAPPIST-1 for an average of ~50 minutes per orbit out of the ~95 minute orbital duration. The observation of a transit during an *HST* visit is typically based on 4 or 5 orbits. Due to the small transit durations of the TRAPPIST-1 planets, only one window per visit covers a transit. Yet, although the transit durations of TRAPPIST-1 planets are short, they have roughly the same duration of *HST*'s observation window, leading to a small (and at times negligible) constraint on the baseline level from the in-transit orbit. As *HST*/WFC3 spectrophotometric observations are affected by orbit-dependent systematic effects, such a limited constraint on the baseline level from the orbit constraining the transit depth can result in a diluted or amplified monochromatic transit depth. The current measurements are particularly limited in such joint "transit depth—baseline level" measurements for planet b (see Figure 1 of de Wit et al. 2016) and planet d (see Figure 1 of de Wit et al. 2018)—and reduced for planets c and e—which is consistent with the level of discrepancies seen in Figure 2. We also note that the transit depth measured for planet f at 0.6 μm (*K2*) is ~3σ shallower than the mean of the other measurements. This measurement could be explained by its low statistical significance (only 6 transits) or by the detrending of *K2* systematic effects and significant stellar variability applied to the light curve before its modeling (see Section 2.1). Nevertheless, there seem to be no significant biases from detrending in the other planet measurements so we would prefer to wait for analyses of additional transits of planet f in this bandpass to confirm or discard this value. For the other planets, no significant chromatic variation is observed. We note that an argument against a stellar contamination origin of the structure visible in the transit spectra of planets b, d, and f, is the absence of similar structures for planets with similar transit impact parameters, i.e., transiting nearly the same chords of the stellar disk.

Figure 3 shows the detrended period-folded photometry measured for each planet observed by *K2* and SPECULOOS, as well as the corresponding best-fit transit model. A visual

Table 6
Transit Timings and Depths Obtained from the Individual Analyses of SPECULOOS Light Curves

Planet	Epoch	Transit Timing [$BJD_{TDB} - 2450000$]		Transit Depth (%)	
b	398	7923.84586	0.00043	0.764	0.060
	406	7935.93284	0.00028	0.842	0.047
	406	7935.93316	0.00053	0.893	0.088
	427	7967.66254	0.00053	0.686	0.068
	431	7973.70588	0.00058	0.759	0.078
	435	7979.74899	0.00030	0.835	0.058
	435	7979.74864	0.00034	0.738	0.048
	439	7985.79209	0.00034	0.721	0.052
	443	7991.83579	0.00041	0.845	0.079
	460	8017.52106	0.00041	0.774	0.079
	462	8020.54219	0.00036	0.758	0.056
	472	8035.65192	0.00065	0.801	0.085
	480	8047.73788	0.00059	0.676	0.094
	507	8088.53228	0.00033	0.796	0.060
	507	8088.53206	0.00026	0.920	0.059
	509	8091.55411	0.00036	0.878	0.065
	509	8091.55364	0.00035	0.809	0.045
	511	8094.57595	0.00067	0.822	0.120
	445	7994.85842	0.00047	0.819	0.084
	445	7994.85833	0.00051	0.855	0.083
c	294	7994.81758	0.0004	0.835	0.068
	294	7994.81885	0.00065	0.695	0.082
	301	8011.77150	0.00046	0.826	0.066
	301	8011.77102	0.00036	0.878	0.078
	310	8033.56743	0.00041	0.801	0.060
	315	8045.67598	0.00035	0.738	0.055
	329	8079.58077	0.00042	0.649	0.055
	329	8079.58172	0.00050	0.679	0.055
	336	8096.53342	0.00037	0.789	0.055
	336	8096.53330	0.00051	0.819	0.062
	322	8062.62794	0.00039	0.727	0.160
d	72	7961.73755	0.00012	0.394	0.057
	74	7969.83771	0.00020	0.264	0.062
	74	7969.83665	0.00100	0.375	0.065
	75	7973.88834	0.00140	0.401	0.062
	90	8034.62829	0.00063	0.405	0.048
e	45	7934.83251	0.00088	0.442	0.046
	45	7934.82990	0.00092	0.417	0.044
	46	7940.93132	0.00049	0.547	0.048
	46	7940.92923	0.00061	0.454	0.055
	53	7983.62886	0.00095	0.522	0.055
	53	7983.62706	0.00053	0.590	0.057
	54	7989.73173	0.00210	0.449	0.065
	54	7989.72916	0.00067	0.458	0.045
f	35	7993.63410	0.00070	0.741	0.074
	40	8039.66021	0.00084	0.639	0.056
g	21	7924.76924	0.00055	0.791	0.051
	24	7961.82599	0.00075	0.723	0.059
	29	7813.60697	0.00200	0.867	0.17
h	16	7962.86330	0.0018	0.372	0.052
	17	7981.63159	0.0016	0.290	0.046
	17	7981.63059	0.0030	0.301	0.046

Note. Each row represents a transit, the first column gives the planet's name, the second column gives the epoch of the transit, the third column gives the mid-transit timing and the corresponding error resulting from the analysis, and the last column gives the transit depth and corresponding error resulting from the analysis.

Table 7
Transit Timings and Depths Obtained from Individual Analyses of *K2* Light Curves

Planet	Epoch	Transit Timing [$BJD_{TDB} - 2450000$]		Transit Depth (%)	
b	277	7741.02841	0.0011	0.959	0.200
	278	7742.54031	0.00120	0.804	0.160
	279	7744.05191	0.00063	0.740	0.095
	280	7745.56254	0.00071	0.721	0.080
	282	7748.58511	0.00071	0.728	0.084
	283	7750.09533	0.00150	0.776	0.110
	284	7751.60539	0.00093	0.799	0.150
	285	7753.11716	0.00064	0.746	0.100
	286	7754.62846	0.00071	0.720	0.089
	287	7756.13952	0.00110	0.775	0.150
	288	7757.64925	0.00098	0.784	0.100
	289	7759.16120	0.00100	0.689	0.080
	290	7760.67229	0.00086	0.743	0.097
	291	7762.18295	0.00090	0.569	0.055
	292	7763.69272	0.00110	0.741	0.130
	293	7765.20352	0.00056	0.843	0.083
	294	7766.71525	0.00074	0.766	0.089
	295	7768.22451	0.00089	0.932	0.180
	296	7769.73779	0.00140	0.666	0.200
	297	7771.24857	0.00140	0.673	0.150
	298	7772.75851	0.00120	0.643	0.120
	299	7774.26913	0.00085	0.889	0.110
	300	7775.78022	0.00099	0.736	0.120
	301	7777.28984	0.00069	0.685	0.085
	302	7778.80191	0.00084	0.632	0.070
	303	7780.31394	0.00058	0.719	0.089
	305	7783.33438	0.00110	0.604	0.082
	306	7784.84448	0.00150	0.555	0.110
	311	7792.40048	0.00110	0.788	0.092
	313	7795.42062	0.00110	0.902	0.210
	314	7796.93214	0.00093	0.772	0.130
	315	7798.44260	0.00065	0.836	0.120
	316	7799.95368	0.00100	0.822	0.200
	317	7801.46362	0.00099	0.707	0.100
	318	7802.97696	0.00099	0.830	0.280
	319	7804.48723	0.00065	0.783	0.099
	320	7805.99725	0.00110	0.669	0.160
	322	7809.02001	0.00063	0.988	0.120
	323	7810.52858	0.00059	0.809	0.120
	325	7813.55299	0.00079	0.866	0.130
	326	7815.06305	0.00067	0.693	0.073
	327	7816.57407	0.00058	0.851	0.086
c	189	7740.53417	0.00083	0.589	0.091
	190	7742.95370	0.00100	0.737	0.091
	191	7745.37836	0.00200	0.656	0.150
	192	7747.79745	0.00100	0.864	0.150
	193	7750.21906	0.00092	0.699	0.065
	194	7752.64173	0.00100	0.652	0.079
	196	7757.48363	0.00150	0.770	0.160
	197	7759.90355	0.00081	0.552	0.077
	198	7762.32917	0.00098	0.697	0.100
	199	7764.74926	0.00120	0.818	0.120
	200	7767.17041	0.00120	0.791	0.160
	201	7769.59305	0.00082	0.579	0.090
	202	7772.01577	0.00110	0.846	0.081
	203	7774.43531	0.00084	0.732	0.090
	204	7776.85884	0.00084	0.789	0.130
	205	7779.27985	0.00150	0.713	0.110
	206	7781.70135	0.00081	0.785	0.081
	207	7784.12337	0.00080	0.837	0.100
	210	7791.38904	0.00080	0.588	0.086

Table 7
(Continued)

Planet	Epoch	Transit Timing [BJD_{TDB} − 2450000]		Transit Depth (%)	
	211	7793.81167	0.00085	0.674	0.082
	212	7796.23257	0.00072	0.771	0.085
	213	7798.65449	0.00110	0.798	0.140
	214	7801.07700	0.00084	0.771	0.140
	215	7803.49803	0.00100	0.604	0.090
	216	7805.91971	0.00068	0.686	0.080
	217	7808.34120	0.00120	0.797	0.120
	218	7810.76238	0.00210	0.809	0.400
	219	7813.18452	0.00110	0.663	0.071
	220	7815.60631	0.00070	0.856	0.074
d	17	7738.99254	0.00400	0.286	0.110
	18	7743.03818	0.00120	0.564	0.092
	20	7751.14013	0.00180	0.468	0.100
	21	7755.18855	0.00140	0.537	0.120
	22	7759.24739	0.00180	0.461	0.073
	23	7763.28944	0.00130	0.419	0.062
	24	7767.34079	0.00330	0.318	0.130
	25	7771.39074	0.00420	0.453	0.120
	26	7775.44035	0.00180	0.466	0.090
	27	7779.48982	0.00320	0.603	0.240
	30	7791.64154	0.00098	0.570	0.076
	34	7807.84073	0.00570	0.304	0.130
	35	7811.88917	0.00460	0.412	0.210
	36	7815.94153	0.00170	0.361	0.110
e	13	7739.67183	0.00160	0.509	0.100
	14	7745.77293	0.00180	0.514	0.110
	16	7757.96796	0.00310	0.587	0.110
	17	7764.07021	0.00150	0.521	0.120
	18	7770.17149	0.00240	0.447	0.130
	19	7776.26457	0.00190	0.383	0.075
	20	7782.36274	0.00190	0.430	0.070
	22	7794.56245	0.00180	0.599	0.089
f	8	7745.03067	0.00210	0.613	0.160
	9	7754.23474	0.00140	0.653	0.110
	10	7763.44545	0.00240	0.651	0.130
	11	7772.64854	0.00180	0.461	0.061
	14	7800.27394	0.00220	0.524	0.120
	15	7809.47737	0.00270	0.494	0.090
g	8	7764.19229	0.00180	0.559	0.071
	11	7801.25085	0.00120	0.727	0.100
	12	7813.60698	0.00200	0.867	0.170
h	5	7756.38806	0.00300	0.346	0.058

Note. Each row represents a transit, the first column gives the planet's name, the second column gives the epoch of the transit, the third column gives the mid-transit timing and the corresponding error resulting from the analysis, and the last column gives the transit depth and corresponding error resulting from the analysis.

inspection of all individual transit light curves did not reveal such crossing events either.

3.3. Confrontation with the Stellar Contamination Model of Z18

The strong stellar contamination inferred for TRAPPIST-1 planets by Z18 is based on the model presented by Rackham et al. (2017), which assumes a heterogeneous photosphere composed of unocculted spots and faculae, and is described by the equation

$$\epsilon_{\lambda,\mathrm{s+f}} = \frac{1}{1 - f_{\mathrm{spot}}\left(1 - \frac{F_{\lambda,\mathrm{spot}}}{F_{\lambda,\mathrm{phot}}}\right) - f_{\mathrm{fac}}\left(1 - \frac{F_{\lambda,\mathrm{fac}}}{F_{\lambda,\mathrm{phot}}}\right)}, \quad (1)$$

in which $\epsilon_{\lambda,\mathrm{s+f}}$ is the ratio of the observed transit depth $D_{\lambda,\mathrm{obs}}$ by the nominal transit depth D_λ (i.e., the square of the true wavelength-dependent planet-to-star radius ratio) and represents the stellar contamination at wavelength λ; $F_{\lambda,\mathrm{phot}}$, $F_{\lambda,\mathrm{spot}}$ and $F_{\lambda,\mathrm{fac}}$ refer to the flux of the mean photosphere, spots, and faculae, respectively; and f_{spot} and f_{fac} refer to the unocculted spot- and faculae- covering fractions (Rackham et al. 2018).

The contamination spectrum $\epsilon_{\lambda,\mathrm{s+f}}$ was then multiplied with an assumed wavelength-independent nominal planetary transit depth by Z18 to obtain a transit spectrum whose wavelength dependence is only due to the stellar contamination. Ultimately, they fitted the percentages of spots and faculae covering fractions, as well as their temperatures and that of the mean photosphere, to represent at best the transit spectra of the TRAPPIST-1 planets that they measured from the *HST*/WFC3 presented in de Wit et al. (2016, 2018). The authors chose to combine spectra of several planets, justifying their choice by

Table 8
Transit Timings and Depths Obtained from the Individual Analyses of LT Light Curves

Planet	Epoch	Transit Timing [BJD_{TDB} − 2450000]		Transit Depth (%)	
b	386	7905.71514	0.00088	0.848	0.130
	421	7958.59599	0.00038	0.696	0.062
	425	7964.63878	0.00043	0.830	0.063
	429	7970.68530	0.00051	0.706	0.063
c	270	7936.69651	0.00040	0.721	0.053
	298	8004.50488	0.00052	0.879	0.058
	303	8016.61384	0.00087	0.612	0.090
	319	8055.36295	0.00044	0.765	0.059
	284	7970.60046	0.00085	0.638	0.070
d	86	8018.43071	0.00096	0.353	0.027
e	53	7983.62882	0.00140	0.481	0.075
	56	8032.43398	0.00180	0.475	0.100
h	17	7981.63343	0.00110	0.257	0.035

Note. Each row represents a transit, the first column gives the planet's name, the second column gives the epoch of the transit, the third column gives the mid-transit timing and the corresponding error resulting from the analysis, and the last column gives the transit depth and corresponding error resulting from the analysis.

Table 9
Transit Depths Derived from the Global Analysis of All Transits of Each Planet

Planet	dF_{K2} (%)	dF_{SSO} (%)	dF_{LT}(%)
TRAPPIST-1 b	0.721 ± 0.021	0.760 ± 0.025	0.746 ± 0.036
TRAPPIST-1 c	0.684 ± 0.019	0.736 ± 0.029	0.724 ± 0.027
TRAPPIST-1 d	0.412 ± 0.028	0.354 ± 0.027	0.301 ± 0.071
TRAPPIST-1 e	0.449 ± 0.034	0.453 ± 0.025	0.475 ± 0.054
TRAPPIST-1 f	0.541 ± 0.034	0.672 ± 0.052	/
TRAPPIST-1 g	0.668 ± 0.070	0.755 ± 0.035	/
TRAPPIST-1 h	0.347 ± 0.058	0.321 ± 0.036	0.257 ± 0.035

Note. Observations from *K2*, SSO, and LT were processed independently.

Table 10
Median Values and 1σ Limits of the Posterior PDFs Deduced for the Timings and Depths from Their Global Analyses for SPECULOOS Observations

Planet	Epoch	Transit Timing [$BJD_{TDB} - 2450000$]		Transit Depth (%)	
b	398	7923.84588	0.00043	0.744	0.053
	406	7935.93286	0.00023	0.882	0.040
	406	7935.93286	0.00023	0.904	0.084
	427	7967.66246	0.00054	0.706	0.090
	431	7973.70578	0.00053	0.756	0.066
	435	7979.74887	0.00022	0.852	0.052
	435	7979.74887	0.00022	0.763	0.044
	439	7985.79210	0.00031	0.737	0.047
	443	7991.83581	0.00042	0.864	0.073
	460	8017.52101	0.00061	0.758	0.072
	472	8035.65154	0.00062	0.773	0.073
	480	8047.73785	0.00061	0.788	0.065
	462	8020.54220	0.0004	0.698	0.120
	507	8088.53214	0.00022	0.809	0.051
	507	8088.53214	0.00022	0.932	0.054
	509	8091.55387	0.00026	0.895	0.059
	509	8091.55387	0.00026	0.848	0.041
	511	8094.57599	0.00059	0.82	0.110
	445	7994.85799	0.00055	0.735	0.073
	445	7994.85799	0.00055	0.784	0.078
c	294	7994.81840	0.00034	0.792	0.069
	294	7994.81840	0.00034	0.684	0.078
	301	8011.77116	0.00029	0.800	0.072
	301	8011.77116	0.00029	0.904	0.076
	310	8033.56743	0.00038	0.816	0.061
	315	8045.67601	0.00034	0.73	0.050
	329	8079.58130	0.00030	0.634	0.046
	329	8079.58130	0.00030	0.67	0.044
	336	8096.53332	0.00030	0.813	0.046
	336	8096.53332	0.00030	0.818	0.056
	322	8062.62799	0.00037	0.727	0.051
d	72	7961.73774	0.00130	0.398	0.061
	74	7969.83692	0.00070	0.266	0.044
	74	7969.83692	0.00070	0.376	0.053
	75	7973.88758	0.00150	0.372	0.059
	90	8034.62829	0.00069	0.409	0.050
e	45	7934.83078	0.00065	0.406	0.048
	45	7934.83078	0.00065	0.421	0.038
	46	7940.92999	0.00069	0.540	0.050
	46	7940.92999	0.00069	0.471	0.057
	53	7983.62772	0.00086	0.518	0.047
	53	7983.62772	0.00086	0.553	0.070
	54	7989.72944	0.00075	0.446	0.061
	54	7989.72944	0.00075	0.463	0.049
f	35	7993.63412	0.00084	0.732	0.071
	40	8039.66014	0.00091	0.653	0.055
g	21	7924.76918	0.00140	0.810	0.092
	24	7961.82610	0.00053	0.723	0.036
	29	8060.65579	0.00047	0.758	0.036
h	16	7962.86307	0.0016	0.377	0.050
	17	7981.63147	0.0012	0.291	0.044
	17	7981.63147	0.0012	0.316	0.057

Note. Each row represents a transit, the first column gives the planet's name, the second column gives the epoch of the transit, the third column gibes the mid-transit timing and the corresponding error resulting from the analysis, and the last column gives the transit depth and corresponding error resulting from the analysis.

Table 11
Median Values and 1σ Limits of the Posterior PDFs Deduced for the Timings and Depths from Their Global Analyses for *K2* Observations

Planet	Epoch	Transit Timing [$BJD_{TDB} - 2450000$]		Transit Depth (%)	
b	277	7741.02854	0.00088	0.883	0.16
	278	7742.54031	0.00100	0.755	0.130
	279	7744.05189	0.00060	0.707	0.069
	280	7745.56251	0.00069	0.710	0.069
	282	7748.58503	0.00073	0.725	0.082
	283	7750.09517	0.00130	0.759	0.082
	284	7751.60547	0.00093	0.733	0.099
	285	7753.11697	0.00093	0.702	0.095
	286	7754.62839	0.00068	0.704	0.081
	287	7756.13946	0.00095	0.748	0.120
	288	7757.64914	0.00096	0.787	0.130
	289	7759.16115	0.00095	0.678	0.071
	290	7760.67223	0.00092	0.729	0.084
	291	7762.18186	0.00067	0.798	0.098
	292	7763.69279	0.00130	0.737	0.130
	293	7765.20350	0.00056	0.848	0.082
	294	7766.71535	0.00058	0.754	0.074
	295	7768.22554	0.00086	0.772	0.093
	297	7771.24824	0.00150	0.634	0.110
	298	7772.75842	0.00120	0.628	0.110
	299	7774.26926	0.00093	0.862	0.097
	300	7775.78035	0.00099	0.699	0.110
	301	7777.28988	0.00067	0.679	0.081
	302	7778.80210	0.00086	0.637	0.072
	303	7780.31392	0.00089	0.763	0.099
	305	7783.33449	0.00099	0.590	0.078
	306	7784.84429	0.00200	0.487	0.096
	311	7792.40048	0.00060	0.784	0.090
	313	7795.42063	0.00095	0.829	0.120
	314	7796.93209	0.00087	0.753	0.110
	315	7798.44265	0.00078	0.799	0.098
	316	7799.95390	0.00090	0.758	0.110
	317	7801.46367	0.00093	0.702	0.095
	319	7804.48731	0.00062	0.749	0.076
	320	7805.99734	0.00120	0.623	0.110
	322	7809.01987	0.00050	0.950	0.080
	323	7810.52885	0.00070	0.718	0.072
	325	7813.55233	0.00087	0.767	0.091
	326	7815.06311	0.00069	0.696	0.070
	327	7816.57415	0.00014	0.825	0.170
c	189	7740.53434	0.00071	0.572	0.057
	190	7742.95387	0.00096	0.711	0.085
	191	7745.37552	0.00130	0.602	0.079
	192	7747.79788	0.00100	0.772	0.099
	193	7750.21885	0.00077	0.685	0.058
	194	7752.64222	0.00130	0.620	0.069
	196	7757.48369	0.00120	0.713	0.110
	197	7759.90363	0.00091	0.542	0.087
	198	7762.32938	0.00099	0.662	0.091
	199	7764.74912	0.00160	0.736	0.096
	200	7767.17049	0.00110	0.741	0.076
	201	7769.59284	0.00079	0.549	0.075
	202	7772.01581	0.01000	0.823	0.072
	203	7774.43569	0.00092	0.681	0.068
	204	7776.85852	0.00081	0.715	0.060
	205	7779.27989	0.00120	0.674	0.090
	206	7781.70123	0.00058	0.768	0.060
	207	7784.12346	0.00092	0.795	0.089
	210	7791.38893	0.00084	0.589	0.081
	211	7793.81172	0.00086	0.657	0.081
	212	7796.23247	0.00074	0.746	0.078

Table 11
(Continued)

Planet	Epoch	Transit Timing [BJD_{TDB} − 2450000]		Transit Depth (%)	
	214	7801.07714	0.00150	0.734	0.120
	215	7803.49838	0.00085	0.624	0.078
	216	7805.91962	0.00110	0.606	0.110
	217	7808.34096	0.00140	0.744	0.082
	219	7813.18461	0.00096	0.641	0.065
	220	7815.60652	0.00072	0.825	0.064
d	17	7738.99218	0.00230	0.258	0.065
	18	7743.03815	0.00087	0.562	0.091
	20	7751.14085	0.00230	0.434	0.079
	21	7755.18922	0.00130	0.428	0.072
	22	7759.24736	0.00210	0.441	0.070
	23	7763.28937	0.00140	0.408	0.065
	24	7767.33969	0.00260	0.283	0.070
	26	7775.44044	0.00160	0.454	0.082
	30	7791.64168	0.00088	0.549	0.062
	36	7815.94088	0.00260	0.289	0.070
e	13	7739.67188	0.00610	0.478	0.089
	14	7745.77245	0.00430	0.473	0.072
	16	7757.96794	0.00340	0.572	0.120
	17	7764.06998	0.00120	0.477	0.077
	18	7770.17137	0.00270	0.413	0.071
	19	7776.26467	0.00190	0.365	0.063
	20	7782.36298	0.00170	0.414	0.059
	22	7794.56266	0.00210	0.587	0.092
f	8	7745.03110	0.00230	0.567	0.090
	9	7754.23467	0.00160	0.603	0.069
	10	7763.44538	0.00200	0.636	0.100
	11	7772.64872	0.00220	0.456	0.070
	14	7800.27402	0.00230	0.494	0.088
	15	7809.47707	0.00170	0.484	0.064
g	8	7764.19196	0.00160	0.567	0.068
	11	7801.25070	0.00120	0.707	0.087
	12	7813.60635	0.00140	0.728	0.100
h	5	7756.38806	0.00300	0.346	0.058

Note. Each row represents a transit, the first column gives the planet's name, the second column gives the epoch of the transit, the third column gives the mid-transit timing and the corresponding error resulting from the analysis, and the last column gives the transit depth and corresponding error resulting from the analysis.

Table 12
Median Values and 1σ Limits of the Posterior PDFs Deduced for the Timings and Depths from Their Global Analyses for Liverpool Telescope Observations

Planet	Epoch	Transit Timing [BJD_{TDB} − 245000]		Transit Depth (%)	
b	386	7905.71519	0.00088	0.834	0.120
	421	7958.59605	0.00036	0.687	0.061
	425	7964.63885	0.00044	0.838	0.053
	429	7970.68541	0.00041	0.707	0.062
c	270	7936.69651	0.00035	0.723	0.047
	298	8004.50488	0.00053	0.853	0.054
	303	8016.61367	0.00068	0.605	0.084
	319	8055.36297	0.00047	0.764	0.066
	284	7970.60044	0.00088	0.641	0.070
d	86	8018.43071	0.00096	0.353	0.027
e	53	7983.62906	0.00130	0.476	0.069
	56	8032.43405	0.00190	0.478	0.100
h	17	7981.63343	0.00110	0.257	0.035

Note. Each row represents a transit, the first column gives the planet's name, the second column gives the epoch of the transit, the third column gives the mid-transit timing and the corresponding error resulting from the analysis, and the last column gives the transit depth and corresponding error resulting from the analysis.

the improved signal-to-noise ratio in detecting common spectral features. To enable a straightforward comparison with the Z18 results, we added our measured transit depths of different planets to obtain the same combinations used by Z18.

The transit depth values obtained from our global analysis of *K2*, SSO, and LT transits, plus the values measured at 4.5 μm with *Spitzer* by Delrez et al. (2018), and at 1.1–1.7 μm with *HST*/WFC3 by de Wit et al. (2016) are displayed in Figure 4 for the combination of planets b and c and Figure 5 for b+c+d+e+f+g, superimposed with the best-fit stellar contamination model of Z18. Table 15 gathers the results for those two combinations, as well as the other combination used in Z18 (d+e+f+g).

The expected transit depths from the best-fit stellar contamination model of Z18, integrated over the spectral bands of the observations, are reported in Table 15 for the combination of planets b+c, b+c+d+e+f+g, and d+e+f+g, along with the actual measurements. To compute those values, we multiplied the contamination spectrum $\epsilon_{\lambda,s+f}$ inferred in Z18 by the maximum combined transit depth for the corresponding combination of planets D_{b+c}, measured from *HST*/WFC3 data by de Wit et al. (2016).

As shown in Figure 4 and Table 15, the dramatic drop of the transit depth in the visible predicted by Z18 model is not observed. As a matter of fact, the Z18 predictions for *K2* bandpass are discrepant by more than 10σ from the observations, at ~6.5σ for SSO, at ~3.5σ for Liverpool, and at ~1.4σ for *Spitzer*. The contamination model inferred by Z18 can thus be firmly discarded. It should also be noted that Z18 attributed an inverted water absorption spectral feature to low-significance variations present in their analysis of the *HST* measurements. However, in de Wit et al. (2016) data we do not see significant traces of this inverted water absorption feature (see the zoomed-in box in Figure 4).

Finally, in Z18, the sum of the spot and faculae covering fraction approaches 100% with a spot of size $R_{spot} = (1.63 \pm 0.50) \times 10^3$ km (Rackham et al. 2017), while we know from Delrez et al. (2018) that the chords of transit of the TRAPPIST planets cover at least 56% of a stellar hemisphere. Z18's model should therefore predict a significant number of spot-crossing events with amplitudes of the order of 400 ppm (Rackham et al. 2017). Quantitatively, according to Z18 for T-1b+T-1c we would expect a frequency rate of 18% spot-crossing and 34% of faculae-crossing events. We analyzed all light curves individually, we see comparable variability in and out of transit, at a significantly lower level than expected (maximum 200 ppm), and no asymmetries in the amplitude of the residuals.

While the model of Z18 is discarded by our data, significant stellar contamination of TRAPPIST-1 planets' transmission spectra remains a possibility. Indeed, the star's photosphere is

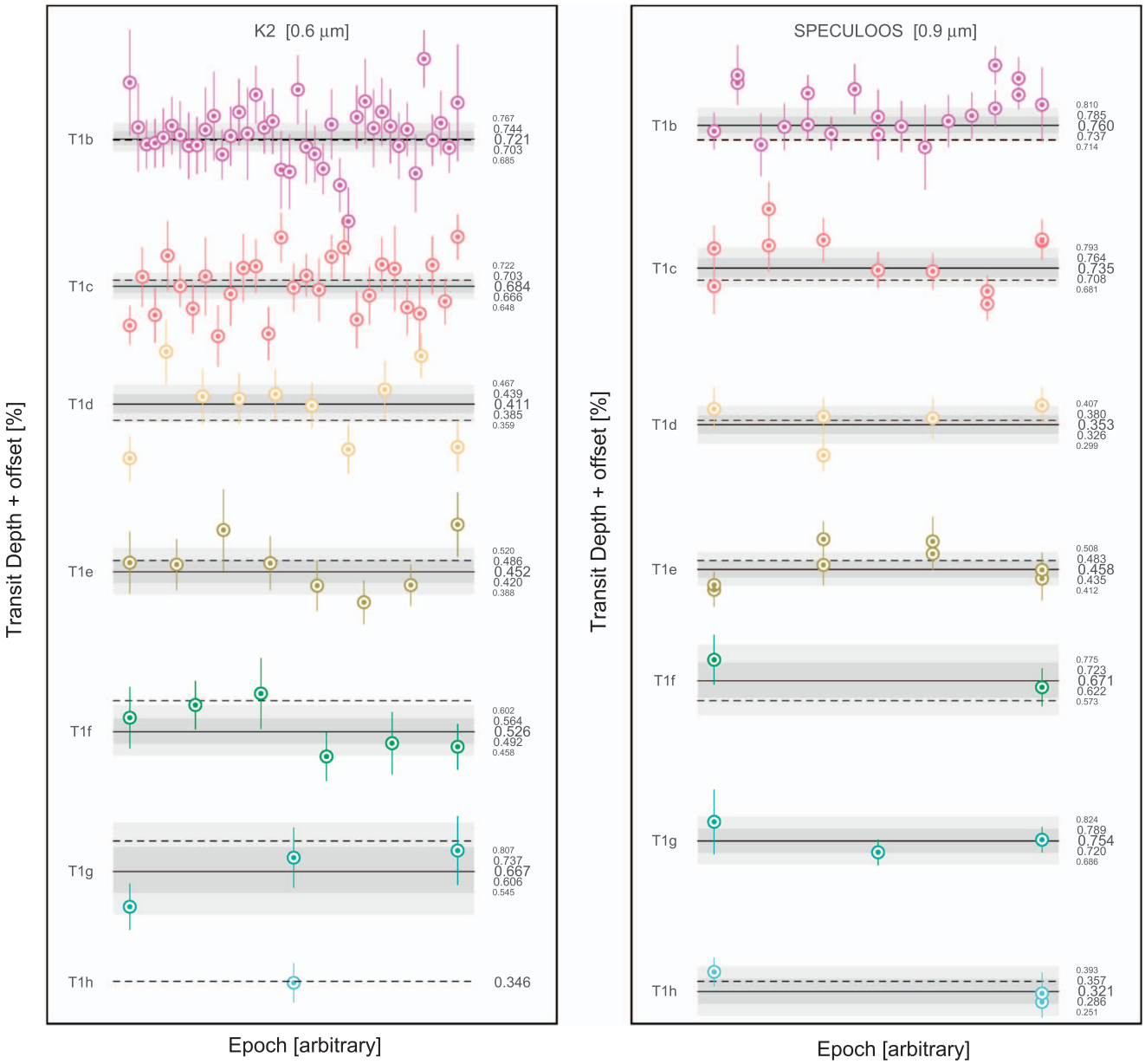

Figure 1. Left: evolution of the measured transit depths from the global analysis of transit light curves gathered by *K2*. The horizontal black lines show the medians of the global MCMC posterior PDFs (with their 1σ and 2σ confidence intervals, in shades of gray), and the dotted lines show the medians of the global MCMC posteriors PDFs for all transits of the same planet observed by *Spitzer*, as reported in Delrez et al. (2018). Events are ranked in order of capture, left to right (but not linearly in time). Right: same as the left panel, but for transits observed with SSO. Neither SSO or *K2* data show significant variability (less than 3σ).

definitely heterogeneous, as its *K2* photometry shows a quasi-periodic variability of a couple percent, with a dominant period of 3.3 days that is consistent with the rotation of an evolving inhomogeneous photosphere (Luger et al. 2017), or with the characteristic timescale between flares followed by spot-brightening (Morris et al. 2018, hereafter M18). The photometry of the TRAPPIST telescope (Gillon et al. 2011) also shows variability of similar amplitude, with a dominant period identified to be ∼1.4 days by Gillon et al. (2016). We note that this latter value is close to the alias of 3.3 days, suggesting that the periodogram analysis done by Gillon et al. (2016) did not identify the right period because of the discontinuous sampling of the TRAPPIST observations, or that the variability is only quasi-periodic.

3.4. On the Possible Photospheric Structure of TRAPPIST-1

3.4.1. Giant Cold Spots?

While not stated explicitly, the photospheric model of Z18 considered solar-like spots + faculae, and not giant spots + faculae, as this is the only way for the percentages obtained for the best fit (∼30% of spots and ∼63% of faculae) to agree to a certain extent with the predictions of R18 on which it is based (8^{+18}_{-7}% of spots and 54^{+16}_{-46}% of faculae). At this point, it is worth explaining what is meant by giant spots and solar spots. The "solar spot" model used in R18 relies on small time-steady rotating spots to produce the predicted variability amplitude in transit depth. As the variations in flux cancel out when the spots rotate onto and off of the visible photosphere, a large

Table 13
Standard Deviation and Mean Errors of the Measured Transit Depths for All Data Sets

Telescope	Planet	# Transits	σ (%)	Mean Error (%)
K2	−1b	40	0.084	0.14
	−1c	27	0.080	0.081
	−1d	10	0.11	0.073
	−1e	8	0.077	0.080
	−1f	6	0.072	0.080
	−1g	3	0.087	0.085
	−1h	1	/	/
SPECULOOS	−1b	20	0.069	0.067
	−1c	11	0.080	0.059
	−1d	5	0.057	0.053
	−1e	8	0.055	0.053
	−1f	2	0.055	0.063
	−1g	3	0.044	0.055
	−1h	3	0.044	0.047
Liverpool	−1b	3	0.087	0.081
	−1c	4	0.102	0.062
	−1e	2	0.087	0.081

Note. There are no values for planet h with *K2* nor planets d, g, h with the Liverpool telescope because we had only one light curve for each of those planets.

Table 14
Depths of Transits Observed Simultaneously by *K2* and *Spitzer* and SPECULOOS and the Liverpool Telescope.

Planet	Epoch	*K2*	*Spitzer*
−1b	318	0.830 ± 0.120	0.751 ± 0.027
	320	0.669 ± 0.160	0.699 ± 0.023
	321	0.988 ± 0.120	0.801 ± 0.028
	325	0.866 ± 0.130	0.732 ± 0.022
	326	0.693 ± 0.073	0.724 ± 0.023
	327	0.851 ± 0.086	0.663 ± 0.021
−1c	215	0.604 ± 0.090	0.672 ± 0.025
	216	0.686 ± 0.080	0.652 ± 0.020
	217	0.797 ± 0.120	0.735 ± 0.035
	218	0.809 ± 0.400	0.674 ± 0.029
	219	0.663 ± 0.071	0.668 ± 0.024
	220	0.830 ± 0.120	0.725 ± 0.024
−1d	34	0.304 ± 0.130	0.384 ± 0.020
	35	0.412 ± 0.210	0.382 ± 0.024
	36	0.361 ± 0.110	0.348 ± 0.019
−1f	15	0.494 ± 0.090	0.648 ± 0.025
−1g	12	0.867 ± 0.170	0.777 ± 0.020
Planet	Epoch	SPECULOOS	Liverpool
−1e	53	0.522 ± 0.055 0.590 ± 0.057	0.476 ± 0.069
−1h	17	0.316 ± 0.057 0.291 ± 0.044	0.257 ± 0.035

number of spots are required to reach the predicted transit depth variation, leading to a large, heterogeneous, but nearly time-steady component. Conversely, the "giant spot" model shows large amplitude variability with small covering fraction, as

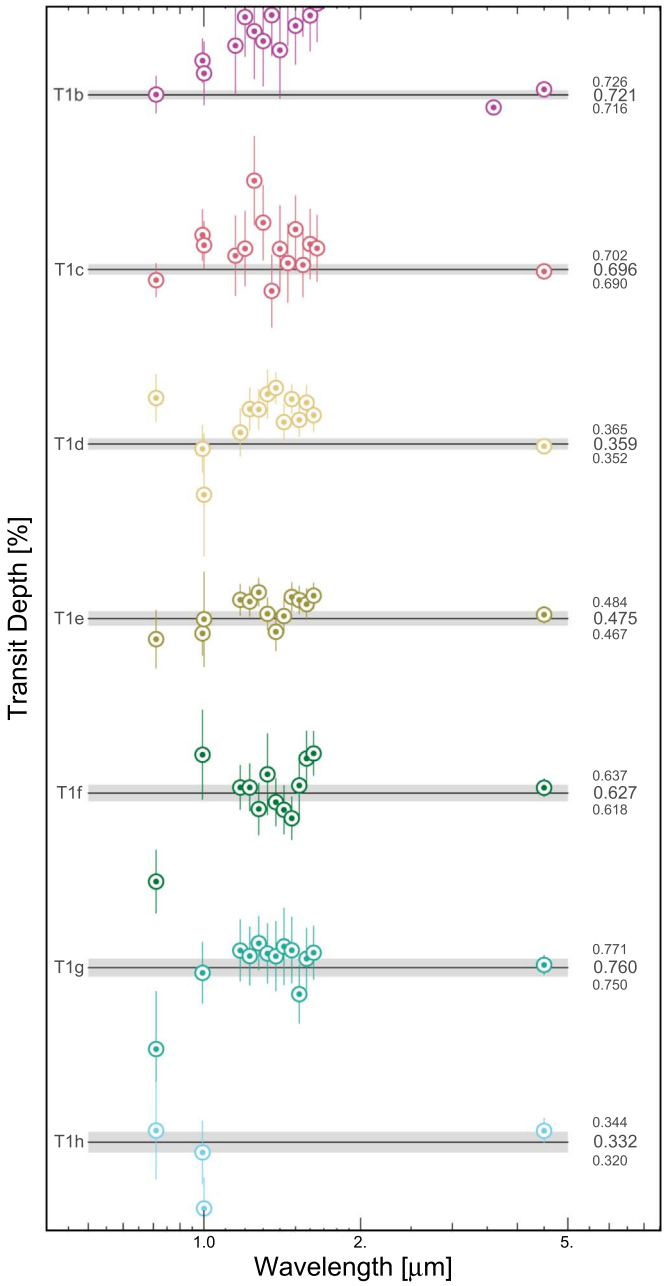

Figure 2. Spectra of the seven TRAPPIST-1 planets. The continuous line is the weighted mean of all non-*HST* measurements for each planet (with its 1σ confidence, in shades of gray). Each point stands for the median of the global MCMC posterior PDF with error bars at the effective wavelength of the instrument (13 points (14 for T1b) per planet: one for *K2*, one for SSO, one for LT, 9 for *HST*/WFC3 and one (two for T1b, 3.6 μm and 4. 5 μm) for *Spitzer*).

there is no cancellation between spots rotating on and off, and giant spots therefore have a variable component.

If instead of considering solar-type spots + faculae, we consider giants spots + faculae, we see that the prediction from the CPAT (composite photosphere and atmospheric transmission) model of Rackham et al. (2017) on the transit depth variations is much less pessimistic (not more than a 0.7% difference between transit depth at 4.5 μm and at 0.6 μm for an M9V type star, R18, Figure 7). We could thus imagine that the photosphere of TRAPPIST-1 is more likely to host giant spots than solar-like spots. In this case it is worth noting that according to the predictions of R18, for Earth-twin type

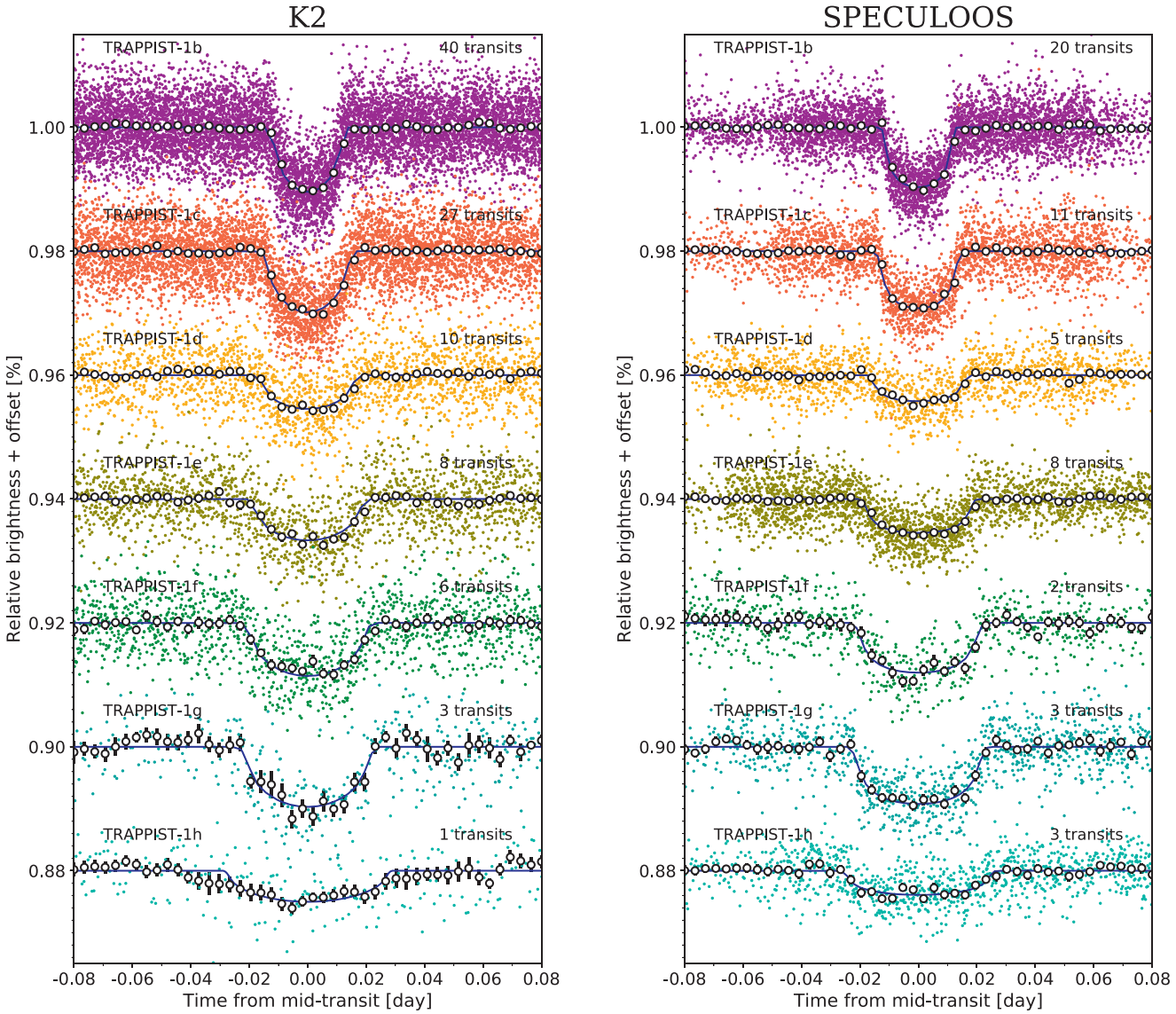

Figure 3. Left: period-folded photometric measurements obtained by *K2* near the transits of the seven planets, corrected for the measured TTVs. The colored dots show the unbinned measurements; the open circles depict the 5-minute binned measurements for visual clarity. The best-fit transit models are shown as dark blue lines. The numbers of transits that were observed to produce these combined curves are written on the plot. Right: same as the left panel but for SSO.

planets, the stellar heterogeneity does not jeopardize the detection of planetary atmospheric features with *JWST* anymore. Considering a precision of 30 ppm with *JWST*, R18 indicates that for a M8V type star like TRAPPIST-1 the depth variations due to atmospheric features should be of the order of 90 ppm, whereas the variations due to stellar heterogeneity should be of the order of ≈17 ppm, consequently allowing detections of planetary features despite stellar contamination.

As discussed above, the TRAPPIST-1 planets cover a significant part of the hemisphere of the star from latitudes up to 30°, latitudes where we find spots on the Sun (Miletskii & Ivanov 2009). The next logical step is to look for giant spot-crossing events in the transits of the TRAPPIST-1 planets. In the observations carried out by *Spitzer* the in and out of transit variability was more likely attributed to systematic effects or granulation variability (see Delrez et al. 2018). Yet the spot-to-photosphere contrast is wavelength-dependent such that spot-crossing events are not detectable at all wavelengths (see Ballerini et al. 2012). However, our analyses of observations in the visible and near-IR carried out by *K2*, SPECULOOS and the Liverpool telescope do not show transit depth variability that could have been attributed to stellar spot crossings during transits (see Section 3.1). A possible scenario allows for giant spots consisting of high-latitude spots that never cross the planets' transit chords, in a similar manner as the circumpolar spots observed for young mid-type to late-type M-dwarfs not older than 1 Gyr (see Barnes et al. 2015); this potentially could explain the variability detected in the *K2* bandpass. However, TRAPPIST-1 is not a young dwarf, its age having been estimated to be 7.6 ± 2.2 Gyr by Burgasser & Mamajek (2017), and the out-of-transit rotational variability resulting from a giant, dark polar spot does not match the small observed variability of 2 ppm (Delrez et al. 2018) seen in the infrared (Morris et al. 2018). In addition, the giant spot model is disfavored by the correlations between flares and spot-brightening seen in the *K2* data set, which indicates that the brightening is not due to spots rotating out of view, but rather

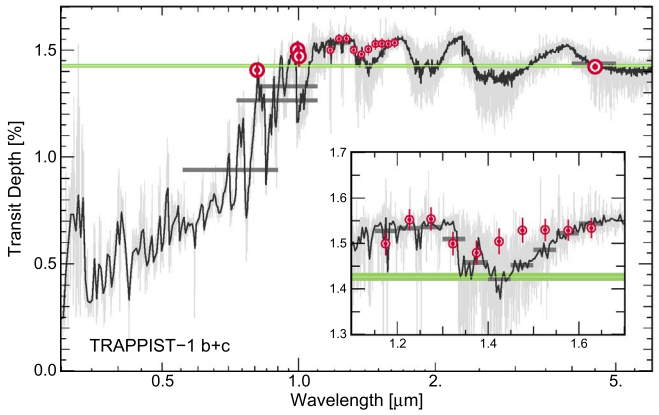

Figure 4. Up: comparison of the stellar contamination spectrum inferred by Z18 for TRAPPIST-1 b+c transits (Zhang et al. 2018) at two different resolutions (continuous black line and gray line) with the *K2*, SSO and LT measurements presented in this work, and the *Spitzer* and *HST*/WFC3 presented in Delrez et al. (2018) and de Wit et al. (2016), respectively (red points). The green line represents the weighted mean of all measurements except *HST* for the reasons outlined earlier in Section 3.2. Finally, the gray horizontal bars are the band-integrated value for the Z18 model on the effective bandpass of each filter (defined as the interval where the product of the filter response and the stellar spectrum is greater than 1%).

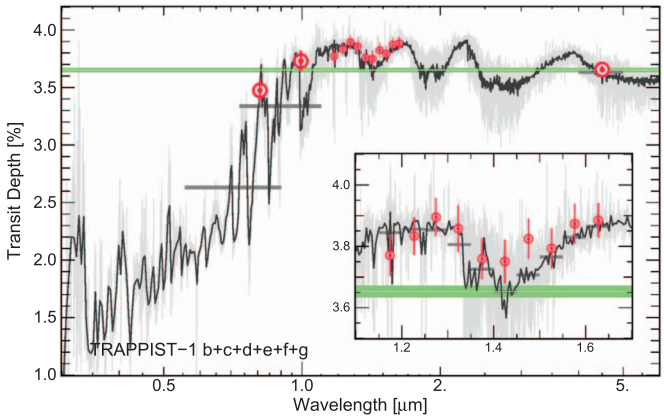

Figure 5. Comparison of the stellar contamination spectrum inferred by Z18 for TRAPPIST-1 b+c+d+e+f+g transits (Zhang et al. 2018) at two different resolutions (continuous black line and gray line) with the *K2* and SSO measurements presented in this work, and the *Spitzer* and *HST*/WFC3 presented in Delrez et al. (2018) and de Wit et al. (2016), respectively (red points). The green line represents the weighted mean of all measurements except *HST* for the reasons outlined earlier in Section 3.2. Finally, the gray horizontal bars are the band-integrated value for the Z18 model where the integrals are weighted uniformly in wavelength.

due to a temporary brightening of the star that follows each flare event (Morris et al. 2018).

3.4.2. Small Hot Faculae?

In their studies, R18 and Z18 assumed that the active regions of TRAPPIST-1 are qualitatively similar to solar active regions in the spot and facular flux contrasts, and in the relative areas of each component. However, there is abundant evidence that the Sun is a poor analog for the starspot distributions of fully convective stars (Donati et al. 2003; Morin et al. 2008, 2010; Barnes et al. 2015), which are likely driven by a different magnetic dynamo process (Donati 2011; Reiners 2012).

Morris et al. (2018) presented an alternative, empirically driven hypothetical spot distribution for TRAPPIST-1, consisting of a few small, bright (hot) spots. The proposed hot spots, which are correlated with the brightest flares, drive the modulation with a 3.3 day period in the *K2* bandpass without generating a corresponding signal in the *Spitzer* 4.5 μm band, in agreement with the observations.

We predict the effect of the hot spots of Morris et al. (2018) at 4500 K on the transit depths of TRAPPIST-1 b and c in Figure 6. These spots produce a nearly flat contamination spectrum for wavelengths $\gtrsim$0.7 μm, and modest flux dilution (shallower transit depths) in the *K2* bandpass. We find that spots with temperatures up to 4500 K are consistent at $\sim 2\sigma$ with the observed transit depths, excluding the *HST* data for the reasons discussed above.

Table 15
Combined Transit Depth Values (in Percent) for b+c, b+c+d+e+f+g, and d +e+f+g, as Predicted from the Best-fit Stellar Contamination Model of Z18, and as Measured from *K2*, SPECULOOS, *HST*/WFC3, and *Spitzer* Observations in Their Effective Bandpasses Relative to an M8 Star Spectrum

Planets	Effective Bandpass (μm)	Z18 (%)	Observations (%)
b+c	4.5	1.44 ± 0.03	1.424 ± 0.008
	1.6	1.54 ± 0.03	1.539 ± 0.028
	1.55	1.52 ± 0.03	1.536 ± 0.033
	1.5	1.49 ± 0.03	1.542 ± 0.033
	1.45	1.45 ± 0.03	1.534 ± 0.040
	1.4	1.42 ± 0.03	1.494 ± 0.037
	1.35	1.46 ± 0.03	1.484 ± 0.034
	1.3	1.51 ± 0.03	1.534 ± 0.035
	1.25	1.54 ± 0.03	1.592 ± 0.033
	1.2	1.53 ± 0.03	1.531 ± 0.028
	1.15	1.53 ± 0.03	1.487 ± 0.039
	0.8–1.1	1.33 ± 0.03	1.470 ± 0.032
	0.73–1.1	1.27 ± 0.03	1.490 ± 0.027
	0.55–0.9	0.94 ± 0.03	1.400 ± 0.020
b+c+d+e +f+g	4.5	3.55 ± 0.06	3.646 ± 0.009
	1.63	3.91 ± 0.06	3.885 ± 0.027
	1.58	3.72 ± 0.06	3.873 ± 0.032
	1.53	3.75 ± 0.06	3.793 ± 0.032
	1.48	3.78 ± 0.06	3.824 ± 0.032
	1.43	3.47 ± 0.06	3.750 ± 0.035
	1.38	3.79 ± 0.06	3.759 ± 0.033
	1.33	3.86 ± 0.06	3.858 ± 0.038
	1.28	3.89 ± 0.06	3.895 ± 0.03
	1.23	3.89 ± 0.06	3.834 ± 0.029
	1.18	3.88 ± 0.06	3.771 ± 0.033
	0.8-1.1	/	/
	0.73–1.1	3.34 ± 0.06	4.370 ± 0.049
	0.55–0.9	2.62 ± 0.06	3.474 ± 0.038
d+e+f+g	4.5	2.19 ± 0.05	2.222 ± 0.010
	1.63	2.37 ± 0.05	2.345 ± 0.023
	1.58	2.27 ± 0.05	2.337 ± 0.027
	1.53	2.28 ± 0.05	2.251 ± 0.027
	1.48	2.29 ± 0.05	2.291 ± 0.025
	1.43	2.13 ± 0.05	2.257 ± 0.029
	1.38	2.30 ± 0.05	2.276 ± 0.028
	1.33	2.34 ± 0.05	2.324 ± 0.033
	1.28	2.35 ± 0.05	2.303 ± 0.025
	1.23	2.35 ± 0.05	2.303 ± 0.026
	1.18	2.35 ± 0.05	2.284 ± 0.027
	0.8–1.1	/	/
	0.73–1.1	2.05 ± 0.05	2.233 ± 0.037
	0.55–0.9	1.66 ± 0.05	2.074 ± 0.044

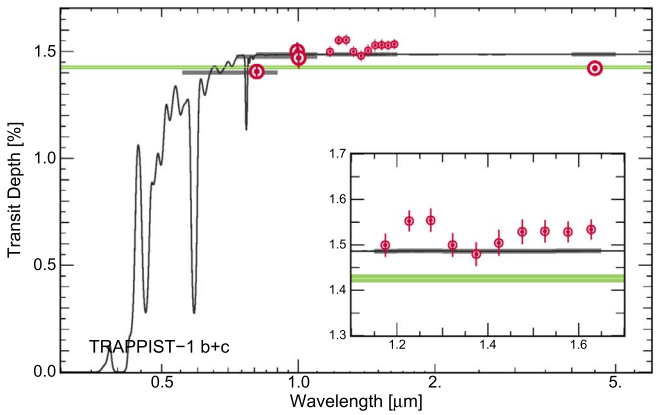

Figure 6. Comparison of the observed transit depth variation (red points) with the predictions from stellar contamination due to the bright spots proposed by Morris et al. (2018) for spots at 4500 K (gray continuous line). We used PHOENIX model atmospheres with photospheric temperature 2511 K and the hot spot properties in M18.

4. Conclusion

We performed individual and global analyses of 169 transit light curves obtained from space with *K2* and from the ground with SSO and LT, as well as the light curves obtained from mid-IR observations with *Spitzer* and the near-IR with *HST*/WFC3 to construct the broadband transmission spectra of the TRAPPIST-1 planets over the 0.8–4.5 μm spectral range. While we could not find any significant temporal variability of the transit depths measured by the same instrument, our analysis reveals chromatic structures at the level of only 200–300 ppm in the transit transmission spectra of planets b, d, and f. These results enable us to discard the highly heterogeneous photospheric model presented by Z18 and their subsequent conclusions regarding the potential of *JWST* to characterize the atmospheric properties of TRAPPIST-1 planets by transit transmission spectroscopy. We identify two possible photospheric structures for TRAPPIST-1 that could agree with our results, one dominated by a few high-latitude giant (cold) spots, which is disfavored for different reasons, and the other by a few small and hot (>4000 K) faculae. Although our measurements do not confirm the conclusions of Z18, they cannot rule out a significant stellar contamination of the planets' transmission spectra. The recent announcement of the delayed launch of *JWST* gives us the opportunity to investigate further the photospheric structure of TRAPPIST-1 —notably through photometric monitoring at different wavelengths—and its impact on the planets' transmission spectra. Furthermore, the *JWST* delay offers more time for the development of new strategies to optimally disentangle the stellar (contamination) and planetary (transmission) effects.

We thank Jon Marchant and Chris Copperwheat for their kind and frequent help in scheduling use of the Liverpool Telescope. The Liverpool Telescope is operated on the island of La Palma by Liverpool John Moores University in the Spanish Observatorio del Roque de los Muchachos of the Instituto de Astrofisica de Canarias with financial support from the UK Science and Technology Facilities Council.

The research leading to these results has received funding from the European Research Council (ERC) under the FP/2007-2013 ERC grant agreement no. 336480, and under the H2020 ERC grant agreement no. 679030; and from an Actions de Recherche Concertée (ARC) grant, financed by the Wallonia-Brussels Federation. This work was also partially supported by a grant from the Simons Foundation (PI Queloz, grant No. 327127), as well as by the MERAC foundation (PI Triaud). L.D. acknowledges support from the Gruber Foundation Fellowship. V.V.G. and M.G. are F.R.S.-FNRS Research Associates. J.d.W. is grateful for the financial support received for the SPECULOOS Project from the Heising-Simons Foundation, P. Gilman, and C. & L. Masson. E.J. is F.R.S.-FNRS. E.A. acknowledges USA NSF grant 1615315, the Guggenheim Foundation, and the NASA Virtual Planetary Laboratory. Senior Research Associate. B.-O.D. acknowledges support from the Swiss National Science Foundation in the form of a SNSF Professorship (PP00P2_163967). A.J.B. acknowledges funding support from the US-UK Fulbright Scholarship programme.

ORCID iDs

B. M. Morris https://orcid.org/0000-0003-2528-3409
M. Gillon https://orcid.org/0000-0003-1462-7739
A. H. M. J. Triaud https://orcid.org/0000-0002-5510-8751
J. De Wit https://orcid.org/0000-0003-2415-2191
E. Agol https://orcid.org/0000-0002-0802-9145
B-O. Demory https://orcid.org/0000-0002-9355-5165
J. Leconte https://orcid.org/0000-0002-3555-480X
D. Queloz https://orcid.org/0000-0002-3012-0316

References

Apai, D., Rackham, B. V., Giampapa, M. S., et al. 2018, arXiv:1803.08708
Ballerini, P., Micela, G., Lanza, A. F., & Pagano, I. 2012, A&A, 539, A140
Barnes, J. R., Jeffers, S. V., Jones, H. R. A., et al. 2015, ApJ, 812, 42
Barstow, J. K., & Irwin, P. G. J. 2016, MNRAS, 461, L92
Burdanov, A., Delrez, L., Gillon, M., & Jehin, E. 2017, arXiv:1710.03775
Burgasser, A. J., & Mamajek, E. E. 2017, ApJ, 845, 110
Claret, A., & Bloemen, S. 2011, A&A, 529, A75
Delrez, L., Gillon, M., Triaud, A. H. M. J., et al. 2018, MNRAS, 475, 3577
de Wit, J., Wakeford, H. R., Gillon, M., et al. 2016, Natur, 537, 69
de Wit, J., Wakeford, H. R., Lewis, N. K., et al. 2018, NatAs, 2, 214
Donati, J.-F. 2011, IAU Symp. 271, Astrophysical Dynamics: From Stars to Galaxies (Cambridge: Cambridge Univ. Press), 23
Donati, J.-F., Collier Cameron, A., Semel, M., et al. 2003, MNRAS, 345, 1145
Eastman, J., Siverd, R., & Gaudi, B. S. 2010, PASP, 122, 935
Gelman, A., & Rubin, D. B. 1992, StaSc, 7, 457
Gillon, M. 2018, NatAs, 2, 344
Gillon, M., Demory, B.-O., Madhusudhan, N., et al. 2014, A&A, 563, A21
Gillon, M., Jehin, E., Lederer, S. M., et al. 2016, Natur, 533, 221
Gillon, M., Jehin, E., Magain, P., et al. 2011, European Physical Journal Web of Conferences, 11, 06002
Gillon, M., Triaud, A. H. M. J., Demory, B.-O., et al. 2017, Natur, 542, 456
Gillon, M., Triaud, A. H. M. J., Fortney, J. J., et al. 2012, A&A, 542, A4
Grimm, S. L., Demory, B.-O., Gillon, M., et al. 2018, arXiv:1802.01377
Howell, S. B., Sobeck, C., Haas, M., et al. 2014, PASP, 126, 398
Luger, R., Sestovic, M., Kruse, E., et al. 2017, NatAs, 1, 0129
Mandel, K., & Agol, E. 2002, ApJL, 580, L171
Miletskii, E. V., & Ivanov, V. G. 2009, ARep, 53, 857
Morin, J., Donati, J.-F., Forveille, T., et al. 2008, MNRAS, 384, 77
Morin, J., Donati, J.-F., Petit, P., et al. 2010, MNRAS, 407, 2269
Morley, C. V., Kreidberg, L., Rustamkulov, Z., Robinson, T., & Fortney, J. J. 2017, ApJ, 850, 121
Morris, B. M., Agol, E., Davenport, J. R. A., & Hawley, S. L. 2018, ApJ, 857, 39
Rackham, B., Espinoza, N., Apai, D., et al. 2017, ApJ, 834, 151
Rackham, B. V., Apai, D., & Giampapa, M. S. 2018, ApJ, 853, 122
Reiners, A. 2012, LRSP, 9, 1
Schwarz, G. 1978, AnSta, 6, 461
Steele, I. A., Smith, R. J., Rees, P. C., et al. 2004, Proc. SPIE, 5489, 679
Stetson, P. B. 1987, PASP, 99, 191
Van Grootel, V., Fernandes, C. S., Gillon, M., et al. 2018, ApJ, 853, 30
Winn, J. N., Holman, M. J., Torres, G., et al. 2008, ApJ, 683, 1076
Zhang, Z., Zhou, Y., Rackham, B., & Apai, D. 2018, arXiv:1802.02086v1